



# Measuring Black Smoker Fluid Flow Rates Using Image Correlation Velocimetry

Timothy J. Crone, William S. D. Wilcock, and Russell E. McDuff  
 School of Oceanography, University of Washington  
 Box 357940, Seattle, WA, USA tjc@ocean.washington.edu

OS31C-1656

## Introduction

A large body of evidence indicates that fluid flow rates within mid-ocean ridge hydrothermal systems may be highly variable [e.g. Baker, 1994; Fornari et al., 1998; Lilley et al., 2003]. And recent studies show that flow within these systems may be strongly sensitive to mechanical forces, such as those generated by seismic activity and tidal loading [Crone and Wilcock, 2005; Johnson et al., 2000]. Thus a wide variety of processes occurring at mid-ocean ridges may be strongly linked through flow variability, including tectonics, tides, chemical exchange, mineral and crustal formation, and biological productivity.

Despite the potential importance of hydrothermal flow variability, no long-term black smoker fluid flow rates have ever been measured. High temperatures, low pH, mineral deposition, and flow disruption all limit the effectiveness of invasive flow measurement techniques for long-term deployments. To address this issue, we are working to develop a technique to measure black smoker fluid flow using video image analysis. Such a technique would allow the non-invasive measurement of black smoker flows, and sea-floor camera systems with this capability would be ideally suited for deployment on a cabled ocean observatory.

As a first step toward developing this technique, we have conducted laboratory simulations of black smoker plumes with known discharge rates, and have applied our correlation-based technique to video imagery of these experiments. We have been able to determine the expected precision of this technique, and have shown that temporally-averaged velocity estimates based on image correlation are linearly related to discharge rate as expected. In its current state, however, our technique correlates noise when applied to faster flow rates, leading to velocity estimates that are lower than expected, as well as reduced sensitivity to flow rate changes. We are now working to develop a better system for weighting individual velocity estimates based on the quality of the correlation.

## Methods

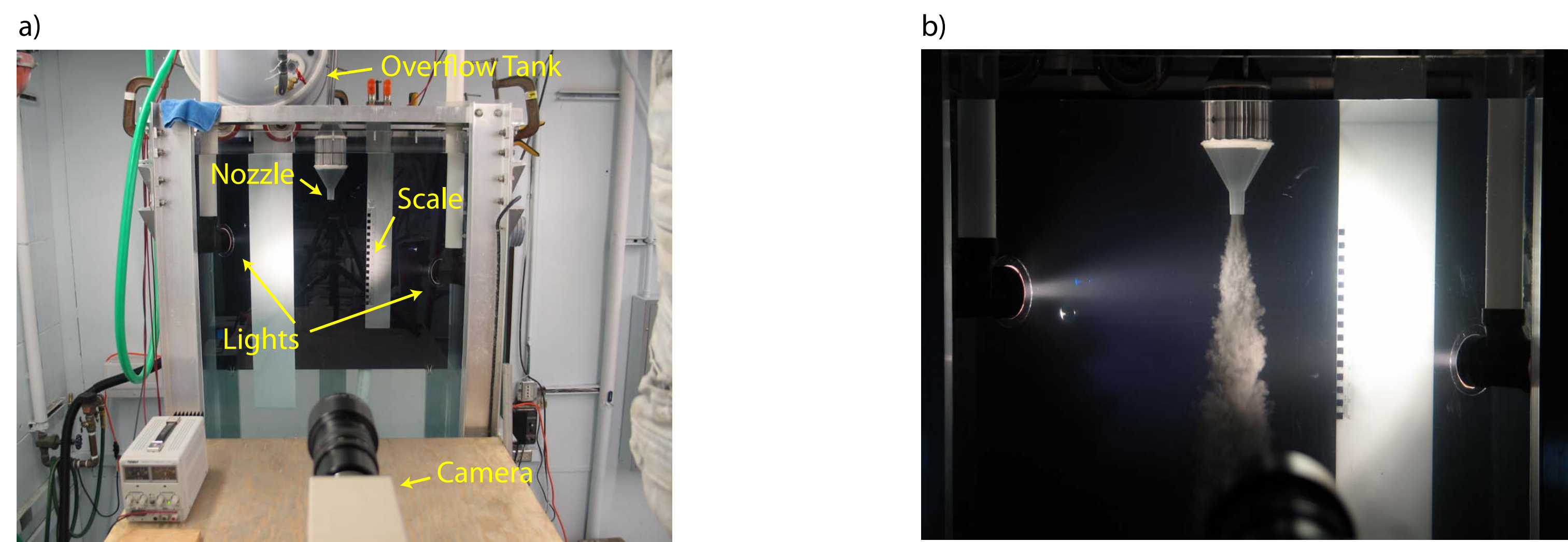


**Figure 1.** Photographs of a) the laboratory apparatus just prior to hydrothermal plume simulation, and b) the laboratory apparatus during plume simulation. To simulate black smoker plumes, we injected water seeded with colloidal graphite through a custom-built flow-straightener and nozzle system into a 2 m-tall 450 gallon tank. We injected the fluid downward, with  $\sim 0.5$  weight-percent NaCl to provide some measure of buoyancy flux, and employed a constant-head overflow tank seen near the top of a), an adjustable head height, and a set of flow restrictors to regulate fluid flow rate. We illuminated the plume with two custom-built underwater halogen flood lights, and recorded the simulations using a NEC TL-22P NTSC video camera (shown), and a QImaging Retiga EX digital video camera. For this poster we analyzed sets of sequences acquired with the QImaging camera at frame rates of 33 frames per second. We conducted five simulations lasting between  $\sim 10$ –15 minutes each, at discharge rates of 2.4, 3.2, 4.1, 5.2, and 5.7 l/min, through an 18 mm nozzle, corresponding to Reynolds numbers of about 2900, 3800, 4800, 6100, and 6700.

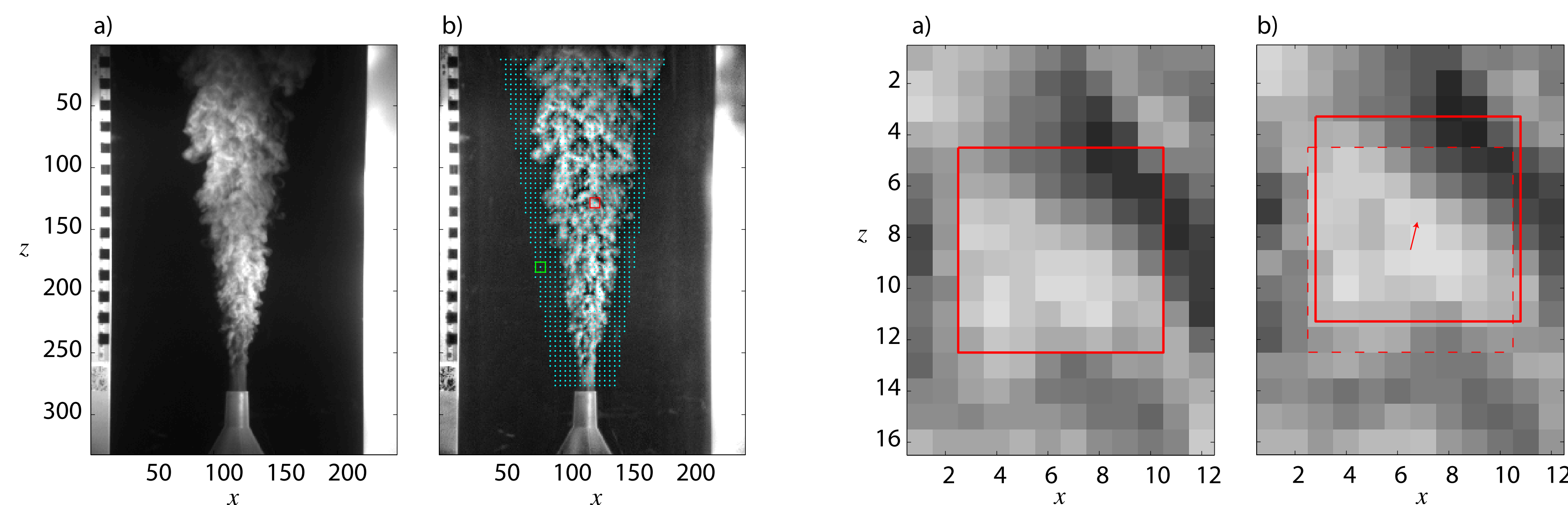


**Figure 2.** A typical video sequence frame shown a) unaltered, and b) after adaptive histogram equalization [Pizer et al., 1987]. For analysis, each image is divided into a set of overlapping subimages with center locations indicated by blue dots in b), and sizes shown by the red and green squares. The scale on the left-hand side of both images comprises 1-cm white and black squares. The approximate resolution of these images at the plume's edge is 8.6 pixels/cm. The red square also indicates the portion of the image expanded in Figure 3. Correlation data from locations indicated by the squares are shown in Figure 4.

**Figure 3.** Subimage regions in a) one video frame, and b) the subsequent frame. The red square in a) indicates the location of the 8 by 8 pixel subimage at time  $t$ , and the squares in b) show the apparent subimage displacement at time  $t + \Delta t$ , determined by minimizing the RMS misfit between the two images. Our technique works best when the frame interval,  $\Delta t$ , is as short as possible, and when subimage sizes are close to the size of the imaged turbulent flow structures.

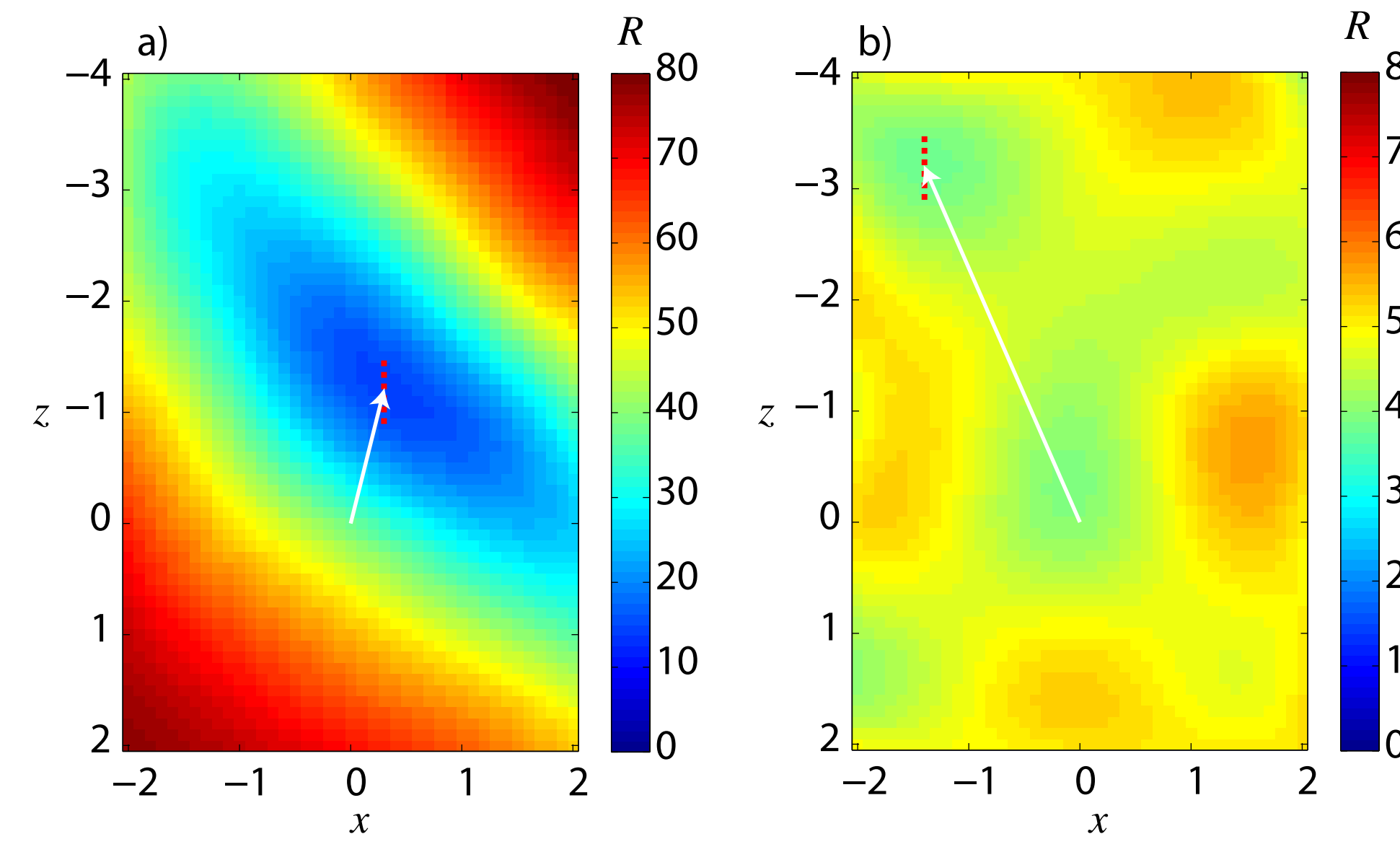


**Figure 4.** Contours of typical spline-interpolated RMS misfit functions,  $R$ , with a) good correlation, and b) poor correlation. Data for a) and b) were taken from image locations shown in Figure 2 with red and green squares, respectively. Arrows indicate subimage displacement vectors determined by the minima. Dashed lines indicate vertical cross-sections shown in Figure 5, which are used to weight the displacement vectors according to the quality of the correlation.

## Statistical Results

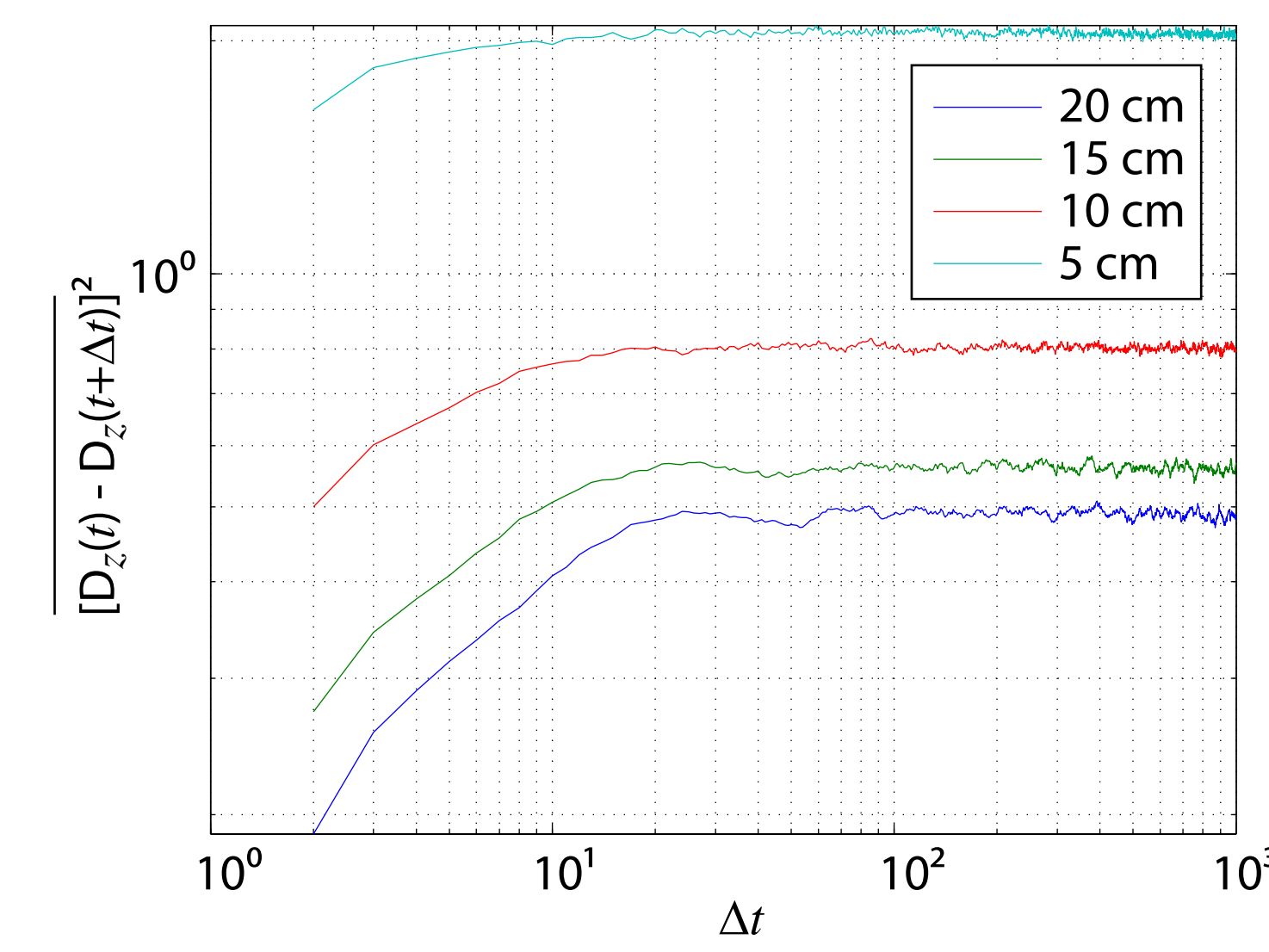


**Figure 6.** Temporal variograms computed at four positions along the centerline of the plume during the 4.1 l/min simulation. The legend provides the locations of these positions in the form of distances from the nozzle. For faster flowing fluid, independent velocity measurements are acquired every  $\sim 4$  frames. For slower fluid, independent measurements are acquired every  $\sim 11$  frames.

**Figure 8.** Contours of the normalized standard error field for a) sample size  $n = 165$  (5 s), and b) sample size  $n = 990$  (30 s). For much of the central portion of the plume, errors are below 10% for  $n = 165$ , and are below 5% for  $n = 990$ . The total population size for this analysis was  $N = 18,873$ , corresponding to a video clip length of  $\sim 9.5$  minutes.

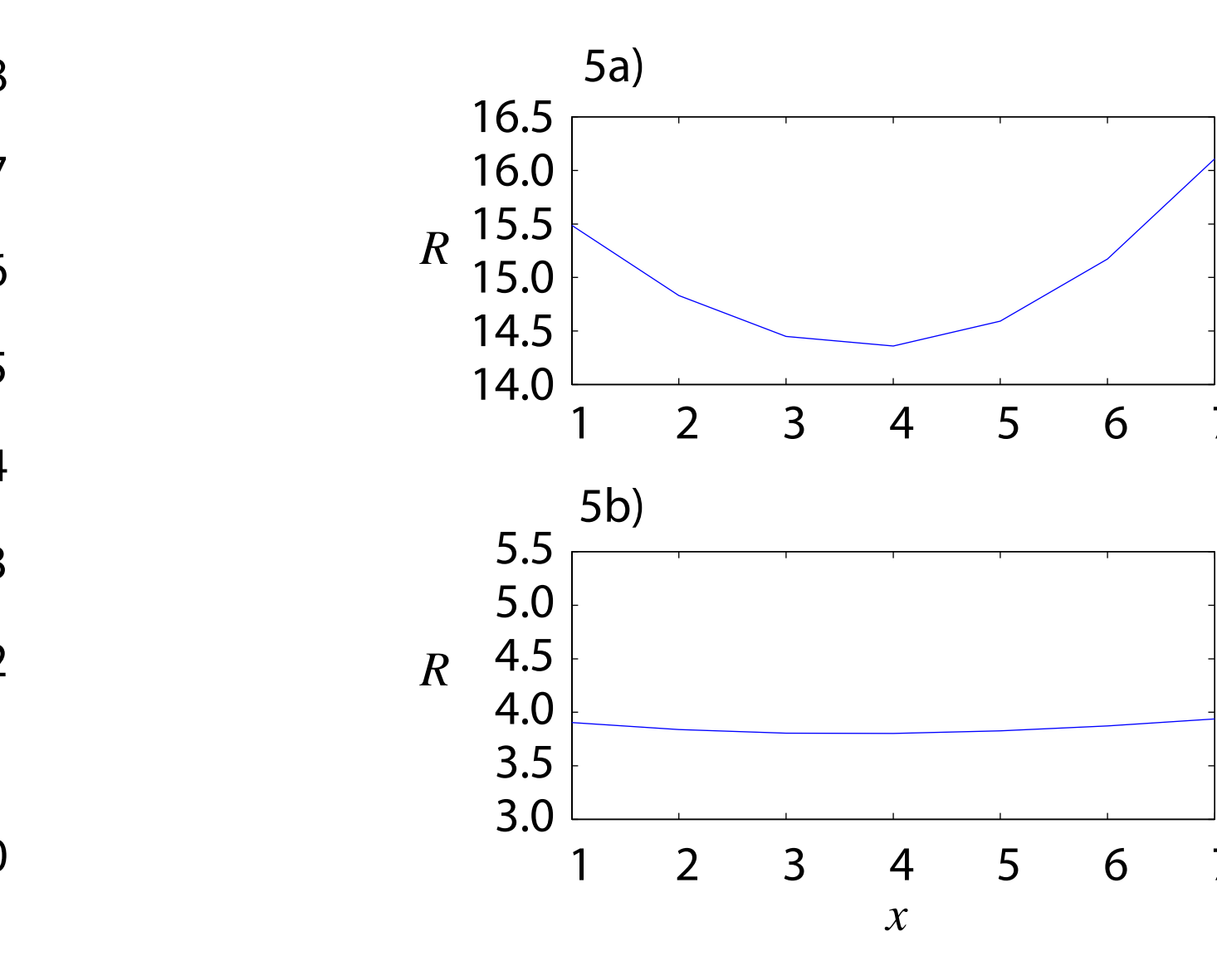
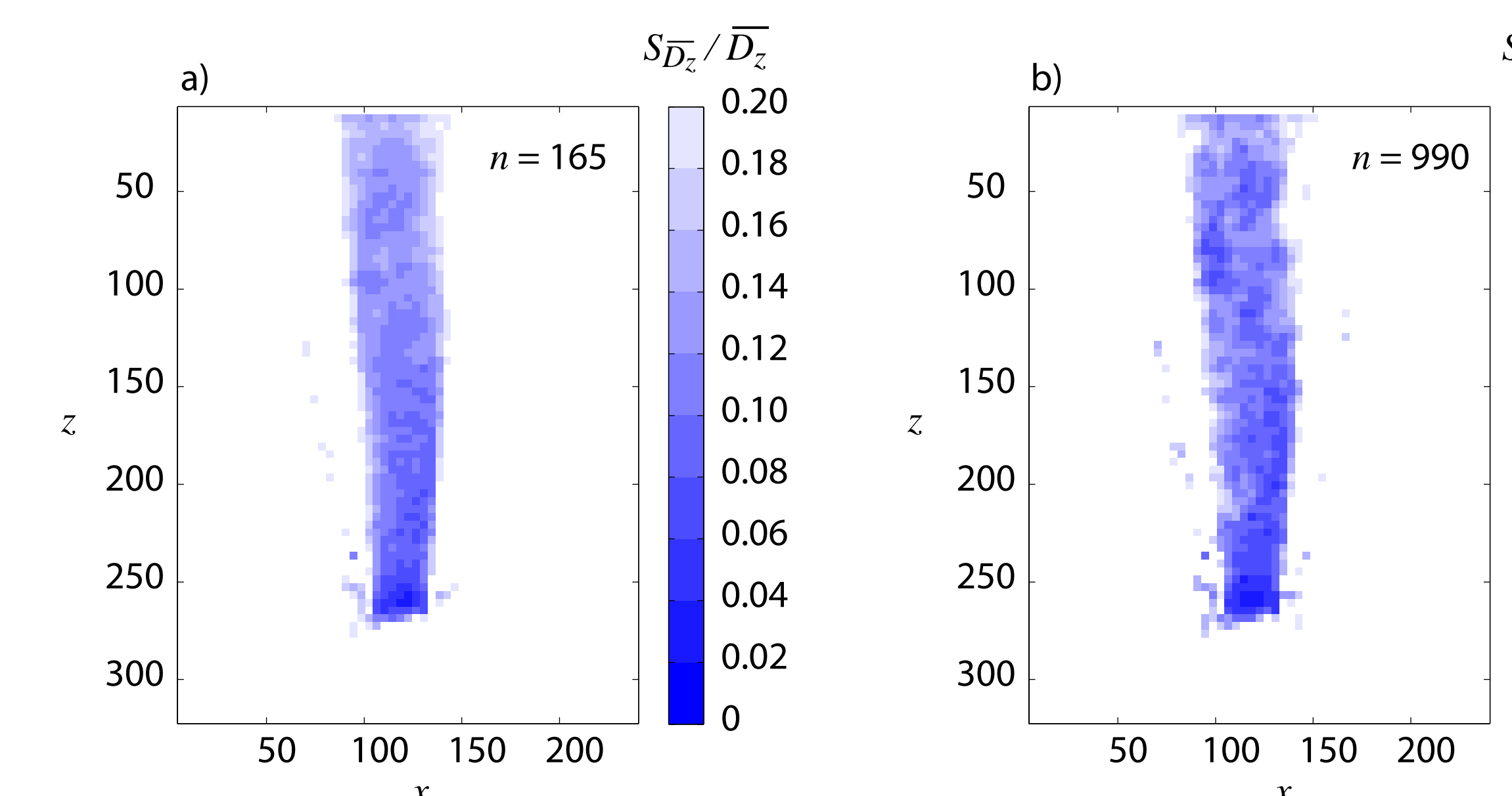


**Figure 5.** Vertical cross-sections around the minima of the misfit functions shown in a) Figure 4a, and b) Figure 4b. We use the slope of the line connecting the misfit minimum to the end values to discriminate good correlations from bad. This scheme is only partially successful at giving low scores to poor velocity measurements, and we are currently searching for a more robust technique.

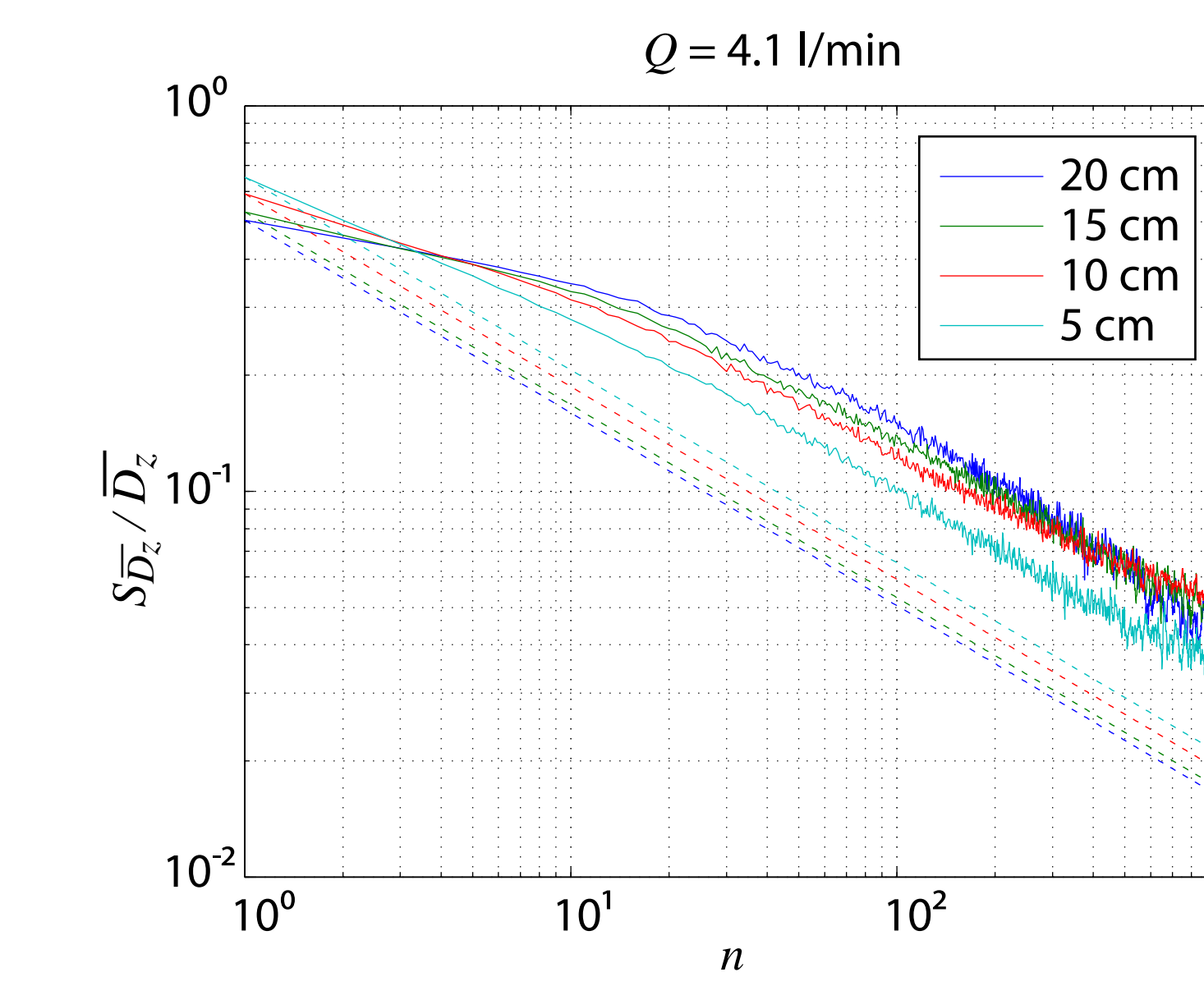


**Figure 7.** The standard error of the mean, normalized by the mean, computed at four positions along the centerline of the plume during the 4.1 l/min simulation. The legend provides the locations of these positions in the form of distances from the nozzle. Dashed lines indicate the theoretical standard error given by the central limit theorem, and solid lines indicate measured standard errors. The two differ because each velocity estimate is not an independent one, as shown in Figure 6. These curves show that, along the centerline, the analysis of a 5-s video clip is accurate to within  $\sim 10\%$ , and the analysis of a 30-s clip is accurate to within  $\sim 5\%$ .

## Velocimetry Results

**Figure 9.** Contours of the two-minute average weighted image velocity fields for the a) 2.4, b) 3.2, c) 4.1, d) 5.2, and e) 5.7 l/min simulations. As the discharge rate increases, the velocity estimates tend to increase, except in the fastest portion of the flow, where noise contaminates the measurements for the faster discharge rates. That is, for faster discharge rates, the imaged turbulent structures undergo more deformation in between frames, driving the noise component of the velocity measurement up. This noise component tends toward zero, and drives the total velocity estimation down. This effect is most pronounced near the nozzle.

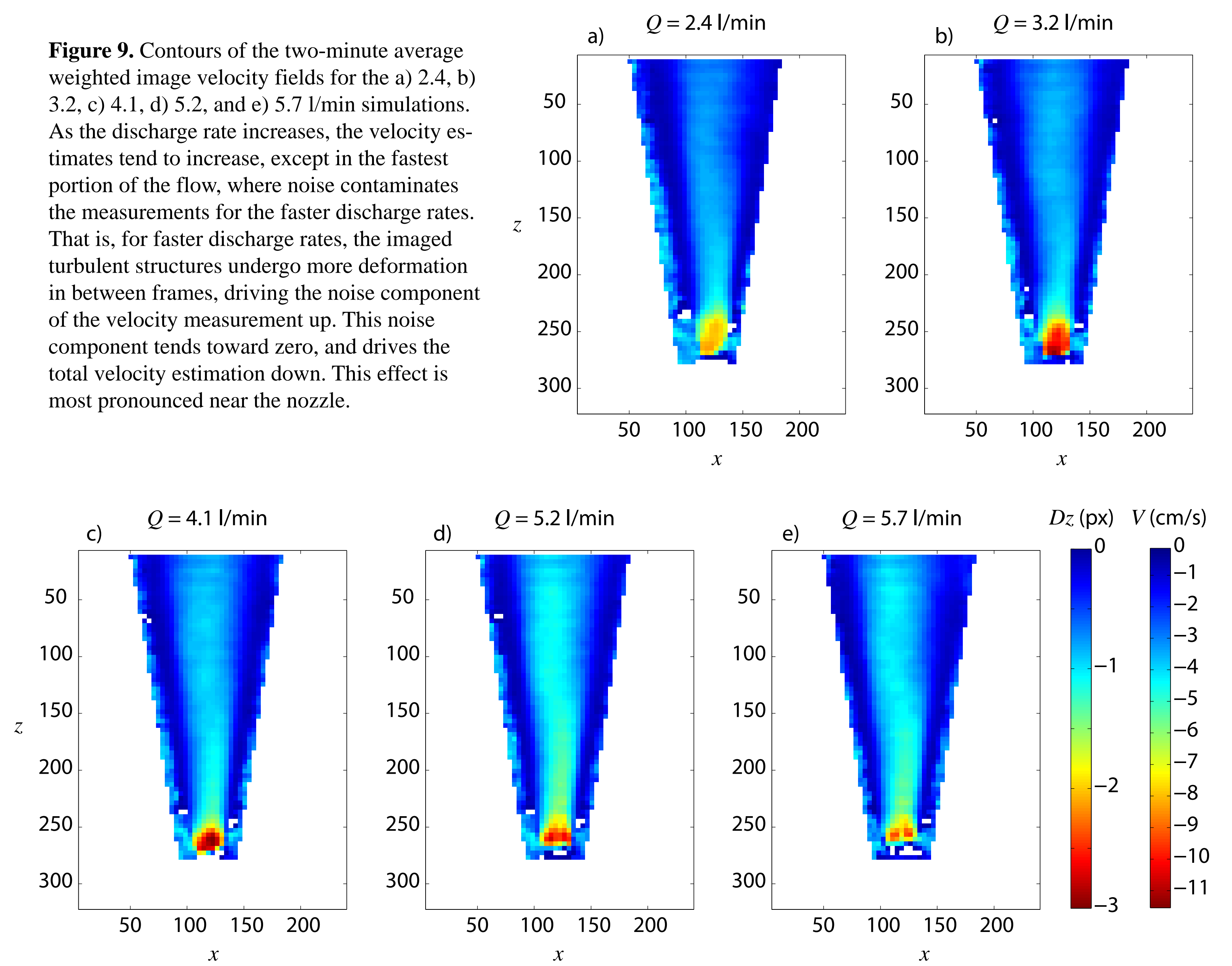
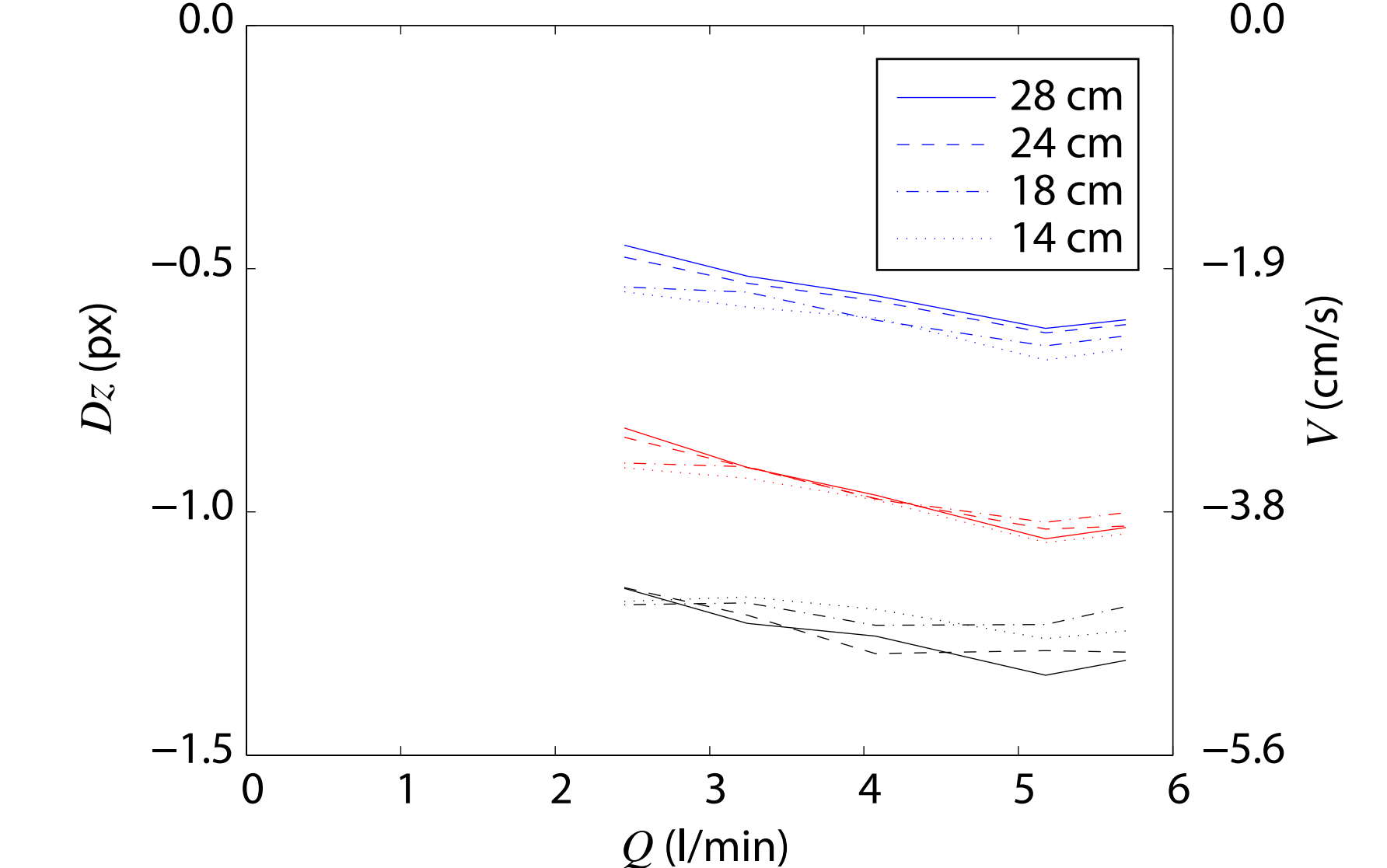


**Figure 10.** Image velocities in the  $z$ -direction averaged across horizontal bands, plotted against fluid discharge rate. Different line styles indicate distance from the nozzle, and line clusters of different color indicate different frame intervals between image pairs used in the analysis. Blue, red, and black lines indicated frame intervals of 1/33 s, 2/33 s, and 3/33 s, respectively. With these curves we can evaluate our technique's ability to appropriately increase velocity estimates for increases in frame interval. At slow discharge rates, doubling the frame interval nearly doubles the velocity, as expected. At higher discharge rates, this is not the case, thus the curves do not trend through the origin. This is a good indication that we are correlating noise at higher flow rates, and a better weighting scheme will need to be developed.



## Future Work

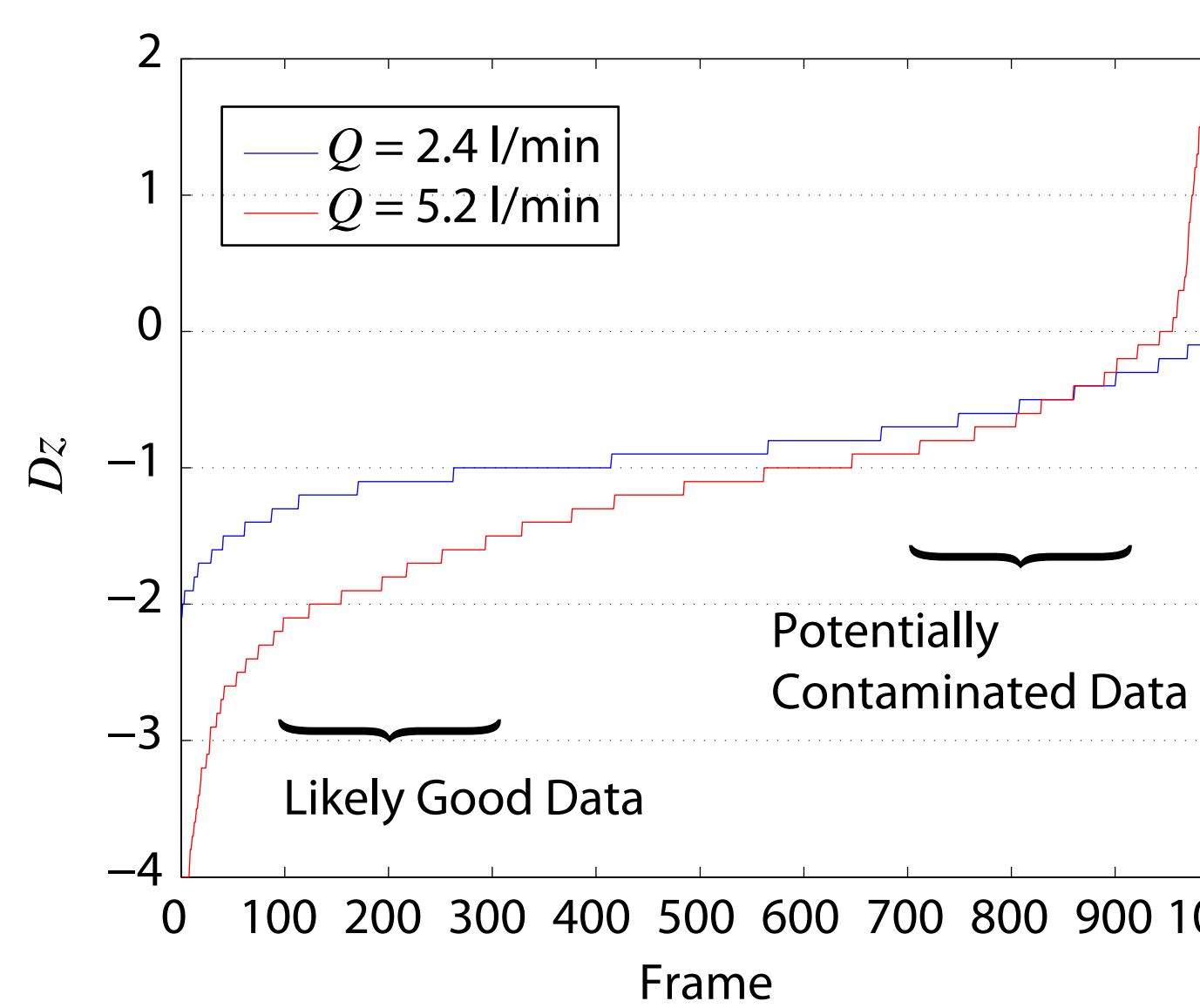


**Figure 11.** Cumulative histogram of image displacements at a single location within the video frame of a 30-s clip from the 2.4 and 5.2 l/min simulations. Here we can see that a large number of velocity estimates generated by our technique for the faster flow are nearly twice as large as those of the slower flow, as expected. However, our technique is not currently capable of discarding or correctly weighting the bad velocity measurements, which leads to poor time-averaged estimates for the faster flows, as seen in Figure 10. We are working toward developing a weighting scheme using information gleaned from the good measurements in these populations.

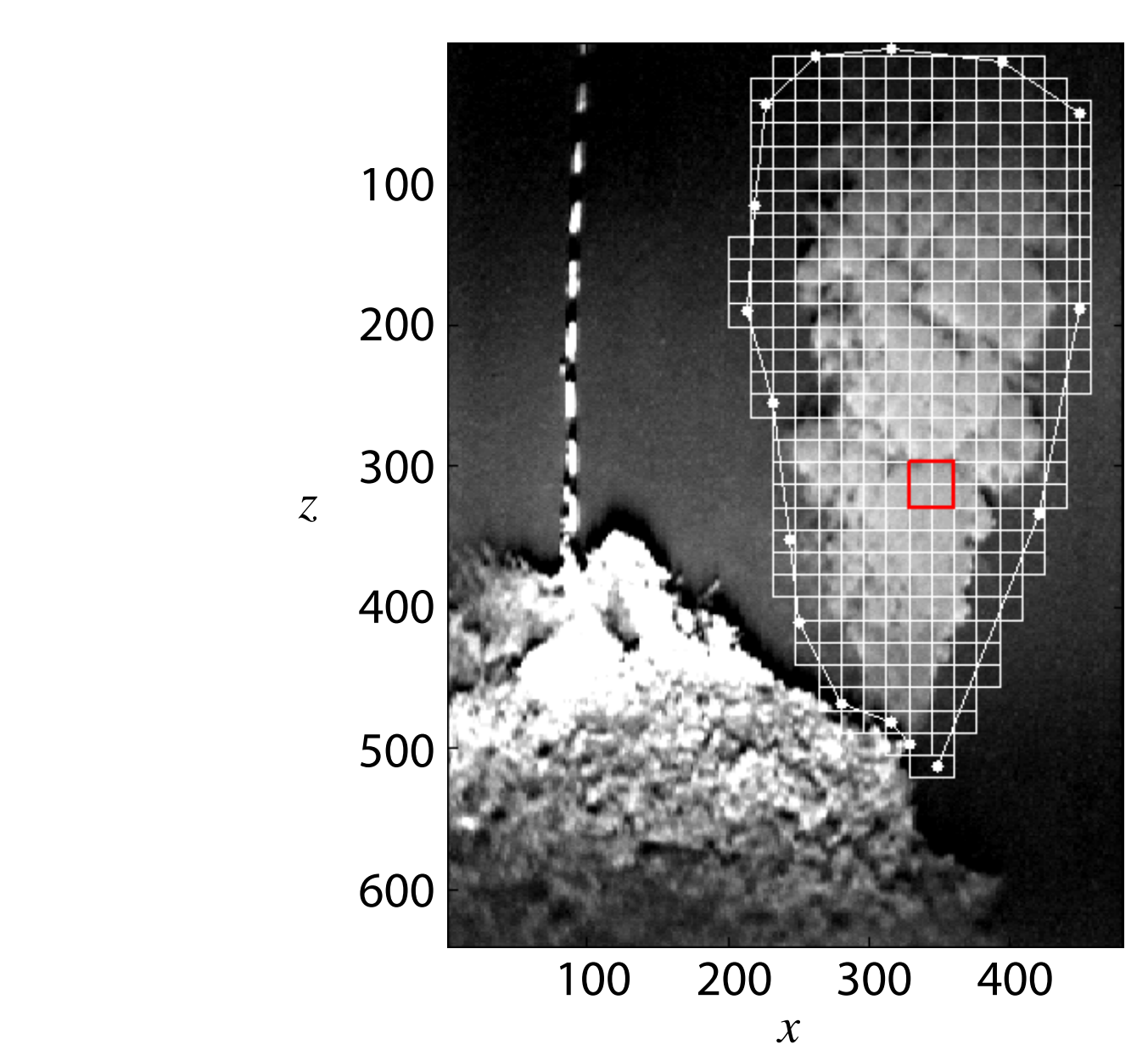


**Figure 12.** Frame capture from video of a seafloor black smoker plume. A series of videos showing flow from this and other black smokers over the course of weeks and months has been previously collected. When we are finished refining our image correlation velocimetry technique, we intend to analyze the seafloor data to look for flow rate changes that might be associated with tectonic activity, which was well-observed during the time-period [Wilcock et al., 2002], or tidal loading, which is predicted to strongly affect flow rates [Crone and Wilcock, 2005]. Such tidal effects on flow have been indirectly inferred through passive acoustic measurements [Crone et al., In Press].

## References

Baker, E. T. (1994) A 6-year time series of hydrothermal plumes over the Cleft Segment of the Juan de Fuca Ridge. *J. Geophys. Res.* **99**, 4889–4904.  
 Crone, T. J., and W. S. D. Wilcock (2005) Modeling the effects of tidal loading on mid-ocean ridge hydrothermal systems. *Geochim. Geophys. Geosyst.* **6**(1) 1–25. doi:10.1029/2004GC000905.  
 Crone, T. J., W. S. D. Wilcock, A. H. Barclay, and J. D. Parsons (In Press) The sound generated by mid-ocean ridge black smoker vents. *PLoS One*.  
 Fornari, D. J., T. Shank, K. L. Von Damm, T. K. P. Gregg, M. Lilley, G. Levai, A. Bray, R. M. Haymon, M. R. Perfit, and R. Lutz (1998) Time-series temperature measurements at high-temperature hydrothermal vents, East Pacific Rise 9° 49'–51' N. *Earth Planet. Sci. Lett.* **160**, 419–431.  
 Johnson, H. P., M. Hutnak, R. P. Dziak, C. G. Fox, I. Urcuyo, J. P. Cowen, J. Nabelek, and C. Fisher (2000) Earthquake-induced changes in a hydrothermal system on the Juan de Fuca mid-ocean ridge. *Nature* **407**, 174–177.  
 Lilley, M. D., D. A. Butterfield, J. E. Lupton, and E. J. Olson (2003) Magmatic events can produce rapid changes in hydrothermal vent chemistry. *Nature* **422**, 878–881.  
 Pizer, S. M., E. P. Amburn, J. D. Austin, R. Cromartie, A. Geselowitz, T. Greer, B. T. H. Romeny, and J. B. Zimmerman (1987) Adaptive histogram equalization and its variations. *Computer Vision, Graphics, and Image Processing* **39**, 355–368.  
 Wilcock, W. S. D., S. D. Archer, and G. M. Purdy (2002) Microearthquakes on the Endeavour segment of the Juan de Fuca Ridge. *J. Geophys. Res.* **107**(B12) 1–21. doi:10.1029/2001JB000505.